Far-infrared magneto-optical study of holes and electrons in zero-band-gap $HgTe/Cd_{0.85}Hg_{0.15}Te$ superlattices

M. Dobrowolska, T. Wojtowicz, H. Luo, and J. K. Furdyna
Department of Physics, University of Notre Dame, Notre Dame, Indiana 46556

O. K. Wu and J. N. Schulman
Hughes Research Laboratories, 3011 Malibu Canyon Road, Malibu, California 90265

J. R. Meyer, C. A. Hoffman, and F. J. Bartoli
Naval Research Laboratory, Washington, D.C. 20375-5000
(Received 26 June 1989)

Far-infrared (FIR) magnetotransmission and magnetotransport measurements have been performed on two $HgTe/Hg_{0.15}Cd_{0.85}Te$ superlattices over a wide temperature region. Three of the six observed resonances are identified as cyclotron resonances of holes and electrons associated with the HH_1 band, and of thermally excited electrons in the E_1 band. Furthermore, the temperature dependence of the electron effective mass and its anisotropy is obtained from these experiments, and an attempt is made to correlate the observed mass behavior with the temperature-induced transition of the superlattices from the zero-band-gap to the open-band-gap regime. Finally, we briefly mention two further FIR resonances observed in the course of these experiments, which are identified as the $1s \rightarrow 2p^+$ transition and as cyclotron resonance of electrons occurring in the CdTe substrate of the superlattice.

I. INTRODUCTION

Type-III superlattices—such as HgTe/CdTe— consist of alternating zero-band-gap and wide-band-gap semiconductor layers. Considerable progress has been made in the past two years toward the understanding of these novel heterostructures.[1-7] In particular, recent investigations[1,8] have demonstrated that such superlattices can exhibit a positive or a negative energy gap at the Γ point, depending on the width of the quantum wells and on the temperature. The negative-gap superlattices are highly complex, exhibiting a striking temperature dependence and a particularly strong sensitivity to the value of the valence-band offset.

When a magnetic field is applied to such structures, the field-induced energy splittings (e.g., the cyclotron-resonance splitting of electrons and holes) correspond to the energy range of far-infrared (FIR) photons. Many *inter* subband transitions in these structures (e.g., those involving the energy differences between the light- and heavy-hole subbands) also correspond in energy to FIR photons. FIR magnetospectroscopy is therefore a particularly sensitive and effective tool for probing the very complicated band structure which characterizes type-III superlattices.

It should be noted that, in addition to their dependence on magnetic field, the FIR spectra of these systems are extremely sensitive to temperature, both because of the thermal excitation of new carriers and because of the rather dramatic changes that take place in the band structure of type-III superlattices as the temperature is varied. For example, for certain layer dimensions a HgTe/CdTe superlattice can be shown to change from a zero-band-gap to an open-band-gap superlattice as the temperature is increased. Frequently the spectrum observed at 4.2 K is *completely different* from that observed at 77 K. Thus the ability to carry out the FIR magnetotransmission experiments on type-III SL's as a function of temperature is of paramount importance.

While the FIR magnetotransmission spectra of type-III superlattices are extremely rich in detail, they are difficult to interpret in isolation, because of the number of processes which occur in the FIR frequency range. The interpretation and identification of transmission features is greatly simplified when the FIR measurements are accompanied by dc galvanomagnetic studies as a function of magnetic field and temperature, since such studies can signal the presence of free carriers—and the sign of their charge, as well as the simultaneous presence of high and low mobility carriers. Such dc transport information is invaluable in identifying the origin of the observed FIR transitions.

In this paper we present the results of a systematic galvanomagnetic and FIR magnetotransmission investigation of two $HgTe/Cd_{0.85}Hg_{0.15}Te$ superlattices, carried out as a function of FIR photon energy, magnetic field, and temperature. Cyclotron resonances of very light holes and two types of electrons are observed and interpreted, and several other transitions are reported.

The paper is organized as follows. In Sec. II we describe the apparatus and the samples used in the investigation. In Sec. III we present the tight-binding band-structure picture of a type-III SL which will be used as a point of departure for discussing the data, and the results

of the galvanomagnetic studies which determine what carriers are present at various temperatures. Finally, in Sec. IV we describe the FIR magnetoabsorption resonances observed on the $HgTe/Hg_{0.15}Cd_{0.85}Te$ superlattices, along with their interpretation.

II. EXPERIMENTAL PROCEDURE

We have performed both far-infrared magnetotransmission and dc transport measurements on two $HgTe/Cd_{0.85}Hg_{0.15}Te$ superlattices grown at the Hughes Research Laboratories in a modified V80H molecular-beam epitaxy (MBE) system. The samples were grown at 170 °C on (100) CdTe substrates. (See Table I).

Superlattice sample No. 1 (ML-28B) has 150 periods of 64-Å HgTe layers and 40-Å $Hg_{0.15}Cd_{0.85}Te$ barriers, while superlattice sample No. 2 (ML-25B) consists of 150 periods of 80-Å wells and 40-Å barriers. The Hg content of the barrier layers was determined to be 15% using energy-dispersive x-ray analysis and photoluminescence.

Far-infrared magnetotransmission measurements on both superlattices were performed at a series of discrete wavelengths in the range between 96.5 and 496 μm. The source of the radiation was an optically pumped FIR laser. The samples were mounted in an optical dewar at the center of a split-coil 60-kG superconducting solenoid. The FIR experiments were performed in the temperature range $5\ \mathrm{K} \leq T \leq 200\ \mathrm{K}$, where the temperature of the sample was monitored by a carbon-glass resistor placed next to the sample.

In order to reduce the signal noise due to FIR power fluctuations, the FIR beam was split into two beams by a beam splitter. One beam was directed to a pyroelectric detector, which provided a voltage signal proportional to the output power of the FIR laser. The other beam was directed to the sample, and the signal transmitted through the sample was detected by a silicon bolometer placed in a separate dewar outside the superconducting magnet. The signals from the pyroelectric detector and from the Si balometer were amplified by two lock-in amplifiers connected to an IBM-AT-compatible computer, and the ratio of the two signals was used in the data analysis.

The measurements were carried out in both the Faraday geometry ($\mathbf{B}\|\mathbf{k}\|\hat{\mathbf{z}}$, where $\mathbf{B}$ is the magnetic field, $\mathbf{k}$ the FIR wave factor, and $\hat{\mathbf{z}}$ is the superlattice growth direction) and the Voigt geometry ($\mathbf{B}\perp\mathbf{k}\|\hat{\mathbf{z}}$), using circularly polarized waves in the former and linearly polarized waves in the latter configuration. The circular polarizations are designated as follows: that polarization which elicits cyclotron resonance *of electrons* is designated as "cyclotron resonance active" (CRA), and the opposite circular polarization is designated as "cyclotron resonance inactive" (CRI). In the Voigt geometry the electric field $\mathbf{E}$ of the linearly polarized FIR waves was either parallel to the magnetic field $\mathbf{B}$ ("ordinary Voigt") or perpendicular to $\mathbf{B}$ ("extraordinary Voigt"). We have also carried out some measurements where $\mathbf{B}$ is at an angle θ to the growth direction between the Faraday and the Voigt configurations.

Van der Pauw Hall and conductivity measurements were performed as a function of magnetic field up to 70 kG, at temperatures ranging between 4.2 and 300 K. The samples were mounted in a Janis Super-Varitemp dewar, which contained a 7-tesla superconducting magnet. Hall and conductivity voltages were averaged over all combinations of contacts and polarities of bias current and magnetic field. Automatic control of the temperature, magnetic field, and bias conditions was accomplished using a data acquisition and processing system interfaced to a Digital Equipment Corporation MicroVax computer. The Ohmic nature of the contacts was verified using an *I-V* curve tracer and checked by performing all measurements at more than one bias current between 1 and 10 μA. No significant dependence of the transport data on bias current was observed. Acquisition of Hall and conductivity data as a function of magnetic field affords the possibility of a detailed multicarrier analysis which yields accurate electron and hole densities and mobilities for the various carrier species present.

III. THEORY AND GALVANOMAGNETIC DATA

A. Band structure of the $HgTe/Hg_{0.15}Cd_{0.85}Te$ superlattices

We now briefly discuss theoretical band-structure results for a type-III superlattice, obtained using the formalism developed by Schulman and Chang.[9] The model is based on a multiband tight-binding theory which includes strain. Assuming a valence-band offset of 350 meV, Hoffman *et al.*[1] found that this model successfully explains magnetotransport results obtained on a series of HgTe/CdTe superlattices with a wide range of well thicknesses. We note parenthetically that early magneto-optical measurements[10,11] appeared to suggest a small valence-band offset (ca. 40 meV). Recently, however, Johnson *et al.*[12] proposed a possible explanation which successfully reconciles the experimental data of Refs. 10 and 11 with a large band offset value.

Figure 1 shows calculated in-plane (k_x) and

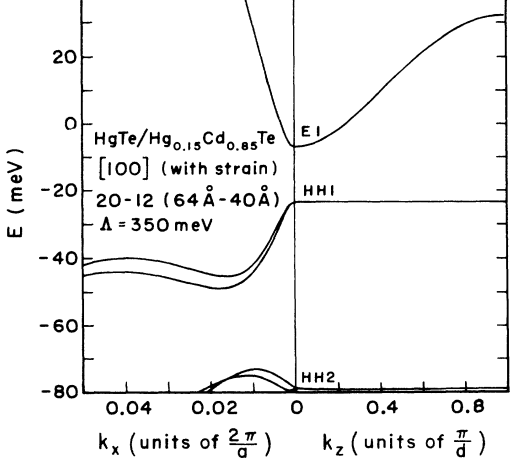

FIG. 1. Superlattice in-plane (k_x) and growth-direction (k_z) dispersion relations for a slightly positive Γ-point energy gap (at $T=0$). The zero point in energy corresponds to the valence-band maximum in *unstrained* HgTe.

growth-direction (k_z) dispersion relations for $HgTe/Hg_{0.15}Cd_{0.85}Te$ superlattice with well and barrier thicknesses the same as those of SL sample No. 1: $d_w = 64$ Å and $d_b = 40$ Å. This superlattice, which has a Γpoint energy gap (E_1-HH_1) of only 16 meV, is seen to have very small in-plane electron and hole effective masses near $k_x = 0$. Although the electron mass is also light in the growth direction ($m^*_{nz}/m_0 \approx 0.014$), the holes are predicted to be almost dispersionless along the z direction. Since there is no single maximum in k_z, holes will populate states along the entire k_z axis in the figure. Furthermore, the in-plane mass m_{px} for a given value of k_z is roughly proportional to the energy gap at that k_z. Hence, the band structure shown in Fig. 1 implies that even in the limit of low temperatures and low doping levels, the highest valence band will contain coexisting holes with a wide range of in-plane effective masses corresponding to different values of k_z.

Figure 1 also clearly shows that the HH_1 valence band is characterized by an extreme nonparabolicity of the in-plane dispersion. For the case illustrated in the figure, the in-plane transport mass $m^*_x \equiv \hbar^2 k(dk/dE)$ increases from less than $0.003m_0$ at a point 3 meV below the top of the valence band to essentially infinite mass at energies only 20 meV farther down. Thus, the holes in narrow-gap and zero-gap (see below) Hg-based superlattices probably have a stronger nonparabolicity than free carriers in any other known material.

Increasing the well thickness from that used in Fig. 1 causes the E_1 (originally electron) and the HH_1 (originally hole) bands to cross. The band structure for a superlattice in this regime is shown in Fig. 2 for $d_w = 80$ Å and $d_b = 40$ Å, the same as for SL sample No. 2. We note from Fig. 2 that the band structure is now much more complicated than that of Fig. 1. At and near the Γ point we speak of a "negative energy gap," in that the energy of the E_1 band (which now determines the top of the valence band of the superlattice in that region of the Brillouin zone) is below the energy of the HH_1 band (which defines the bottom of the conduction band in the vicinity of the Γ point, as shown.) The most striking new feature is the anticrossing of the valence and conduction bands at some finite value of k_z (which we refer to as k_{zc}). This is a consequence of the crossing of the E_1 and the HH_1 bands at that point. At values of k_z above k_{zc} (including $k_z = \pi/d$) the bottom of the conduction band is E_1 in character, the top of the valence band has the HH_1 character, and the superlattice has a positive energy gap in that region of the Brillouin zone.

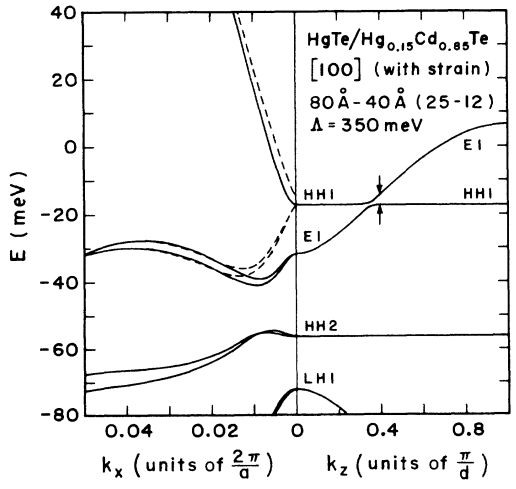

FIG. 2. Superlattice in-plane (k_x) and perpendicular (k_z) dispersion relations for a negative Γ-point energy gap (at $T = 0$). The dashed curves show the in-plane electron and hole dispersion for $k_z = 0.45\pi/d$ (corresponding to the arrows).

This situation effectively results in a *zero energy gap* for the superlattice at $k_z \approx k_{zc}$. Although the actual gap between the bottom of the conduction band and the top of the valence band is very near zero at that point, it is now *indirect*. Furthermore, the valence-band maximum is no longer degenerate over the entire k_z axis (as it was in Fig. 1), but only over the range $k_{zc} < k_z \leq \pi/d$. Note also, in contrast to Fig. 1, that the conduction-band minimum is now degenerate between 0 and k_{zc}. The in-plane electron effective mass (m_x) is therefore now expected to vary strongly with k_z. The dashed curves in the figure illustrate the k_x dispersion relations for electrons and holes with k_z near k_{zc} (the point marked by arrows). Because of these features, we shall refer to superlattices characterized by the type of band structure shown in Fig. 2 as zero-gap superlattices.

The hole effective mass near k_{zc} is seen to be quite small, having an in-plane dispersion which differs markedly from that at $k_z = 0$. Furthermore, near $k_x = 0$ the dashed hole band is even more nonparabolic than that in Fig. 1. Another feature emerging from both Figs. 1 and 2 is that there are also hole states with very heavy masses (see, e.g., the maximum centered at $k_x \approx 0.035$). In Fig. 2 these lie only 11 meV below the top of the band. The calculated in-plane electron and hole effective masses at the zone center becomes quite small as the Γ-point gap E_g^0 (given by the energy difference between E_1 and HH_1 at the Γ point) approaches zero, being nearly proportional to E_g^0.

Below we summarize the distinctive predictions of the theoretical band structures obtained with an assumed valence-band offset of 350 meV for superlattices whose well and barrier dimensions are such that the low-temperature values of E_g^0 are zero or near zero:

(a) the model predicts extremely light hole and electron in-plane effective masses near $k_x = 0$, with the predicted hole-to-electron mass ratio less than a factor of 2;

(b) very strong nonparabolicity for the highest hole band in the k_x direction is predicted;

(c) the calculation illustrated in Fig. 2 predicts a strong anisotropy of the hole and electron effective masses m_z/m_x, where m_x and m_z are the masses in the plane of the superlattice layers and in the growth direction, respectively.

Furthermore, the above theory predicts the low-temperature Γ-point energy gaps for our specific super-

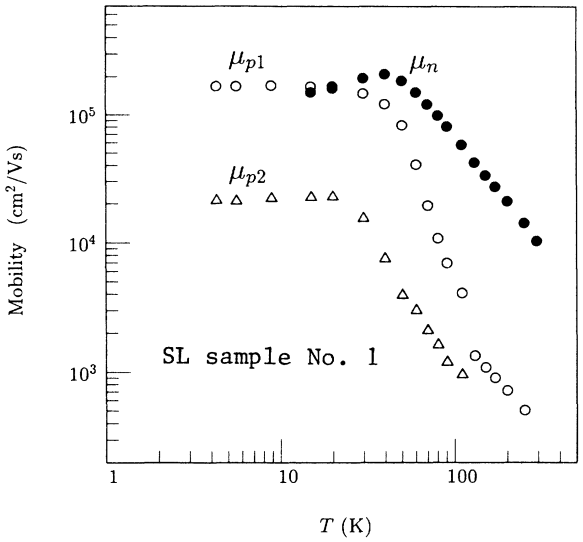

FIG. 3. Experimental electron and hole mobilities vs temperature for SL sample No. 1, as derived from the mixed-conduction analysis of the Hall and conductivity data.

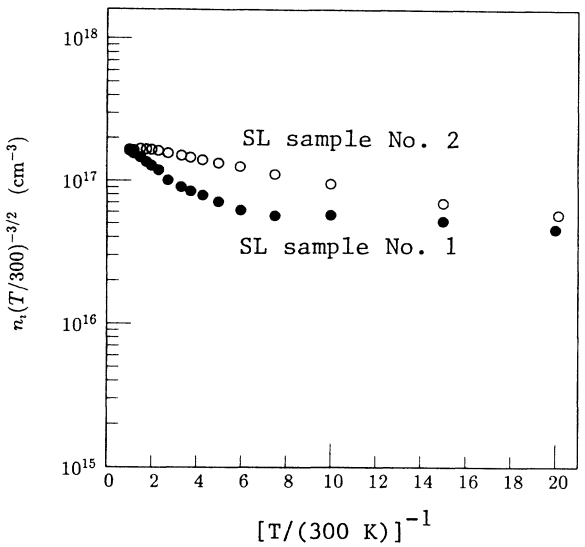

FIG. 4. Experimental intrinsic carrier densities (normalized by $T^{3/2}$) vs inverse temperature for both superlattices. For comparison note the steep slopes obtained for finite-gap samples in Fig. 2 of Ref. 1.

lattices SL sample No. 1 and SL sample No. 2 to be $E_0 = +16$ and -14 meV, respectively.

B. Magnetotransport results

A mixed conduction analysis of magnetotransport experiments carried out on our samples was performed in order to obtain accurate electron and hole densities and mobilities from the magnetic field dependence of the Hall and conductivity data. The analysis employs the conventional assumption that free-carrier mobilities are not appreciably altered by a magnetic field.

For both SL sample No. 2 and SL sample No. 1 superlattices, the Hall data indicate n-type conduction at higher temperatures, but convert to p-type in the low-temperature limit. In the region of p-type behavior the samples show evidence for more than one hole species (for an interpretation of the multiple hole species in terms of "mass broadening," see Ref. 1). In addition, intrinsic electrons were observable over a very broad temperature range, being apparent at temperatures as low as 15 K.

Figure 3 shows experimental mobility results for SL sample No. 1. Temperature-dependent mobilities are given for electrons (μ_n) and for both types of high-mobility holes (μ_{p1} and μ_{p2}). Note that at temperatures below 30 K, μ_n and μ_{p1} are both extremely high ($\approx 10^5$ cm^2/Vs) and the ratio μ_n/μ_{p1} is less than a factor of 2. The extremely high hole mobilities may be explained by small in-plane masses ($\approx 0.001 m_0$), which occur near $k_z = 0$ in very narrow gap superlattices, or near and above k_{zc} in zero-gap superlattices. However, while μ_n shows relatively little dependence on temperature up to 100 K, μ_{p1} falls by over an order of magnitude between 40 and 80 K.

Figure 4 shows that for both samples the quantity $n_i T^{-3/2}$ [where $n_i \equiv (np)^{1/2}$ is the intrinsic concentration] is nearly independent of temperature down to $T = 15$ K. This strongly implies that both superlattices have band gaps of less than ≈ 3 meV. The band-structure theory discussed above is consistent with this implication for SL sample No. 2, but it predicts the value of E_g of $+16$ meV for SL sample No. 1. We will show below that the magnetooptical data also support the conclusion that both samples have a zero band gap at low temperatures, consistent with the transport data. Table I lists maximum mobility values for both samples, as well as theoretical and experimental band gaps.

IV. FIR MAGNETOTRANSMISSION RESULTS AND DISCUSSION

FIR magnetotransmission spectra for both superlattices show a series of distinct absorption lines. In addition, the spectra change very strongly with temperature. There are qualitative similarities—as well as quantitative differences—in the behavior of both superlattices. We describe the observed resonances below, and discuss them in terms of the band structure presented in Sec. III. In addition, SL sample No. 2 exhibits features arising from the specific properties of its substrate. These are presented at the end of this section.

TABLE I. Materials parameters of the samples used.

Sample	d_w (Å)	d_b (Å)	E_g^0 (theory) (meV)	E_g^0 (expt.) (meV)	μ_n^{max} (cm^2/V s)	μ_{p1}^{max} (cm^2/V s)	p_1 (cm^{-3})	μ_{p2}^{max} (cm^3/V s)	p_2 (cm^{-3})
No. 1 (ML-28B)	64	40	16.4	<3	2×10^5	1.7×10^5	7×10^{14}	2.2×10^4	2.3×10^{15}
No. 2 (ML-25B)	80	40	-14.5	<5	7×10^4	6×10^4	2×10^{14}	4×10^3	2.8×10^{15}

A. Low-temperature cyclotron resonance of light holes

Figure 5 shows the magnetotransmission spectra for both superlattices obtained at the laser wavelength $\lambda=229$ μm in the Faraday geometry for both senses of circular polarization. In this geometry the cyclotron orbits are parallel to the HgTe layers of the superlattices. The dominant feature of the spectrum of SL sample No. 1 (64–40 Å) in Fig. 5 is the strong narrow resonant line which appears in the sense of circular polarization for which the hole cyclotron resonance is allowed (CRI). The same line is also observed for SL sample No. 2 (80–40 Å), but with less intensity, for reasons which we present later. We will label this line as resonance "*A*", and we identify it as the cyclotron resonance of holes in the HH_1 band. (The arguments for that interpretation will be given below.) In addition to line *A*, we observe a weak line in the data for SL sample No. 1 in the CRI polarization, labeled as "*B*", and a strong line which appears for both samples in the CRA sense of circular polarization, which we label as resonance "*C*".

The field positions of the two lines observed in the CRI polarization for SL sample No. 1 are plotted in Fig. 6 for all laser wavelengths used in the study. The hole cyclotron resonance (line *A*) extrapolates to the origin in a highly nonlinear fashion, which provides evidence for band nonparabolicity. This nonparabolic behavior of resonance *A* is similar in both superlattices.

Note further that in Fig. 6 the positions of the hole cyclotron resonance plotted as a function of the FIR energy do not lie on a smooth curve. For example, for $\hbar\omega=8.4$ and 6.7 meV the resonance is observed at lower fields than expected from the data at nearby energies (the dashed curve). This observation cannot be accounted for by experimental error. The reason for that is not understood at present, since comparison with theory requires detailed magnetic-field-dependent superlattice band-structure calculations. However, it may suggest "anticrossing" of energy levels (i.e., as the Landau levels increase with field, they may cross some other energy levels and be perturbed in the process).

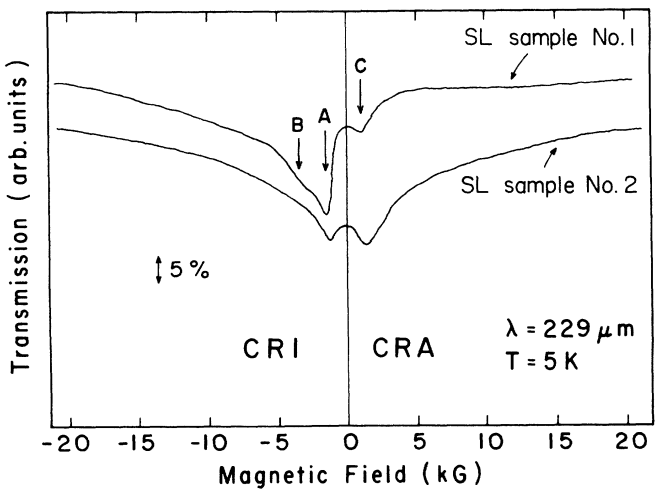

FIG. 5. The FIR magnetotransmission spectra for SL sample No. 1 (64 Å/40 Å) and SL sample No. 2 (80 Å/40 Å) observed in the Faraday geometry at $T=5$ K and $\lambda=229$ μm, for both senses of circular polarization.

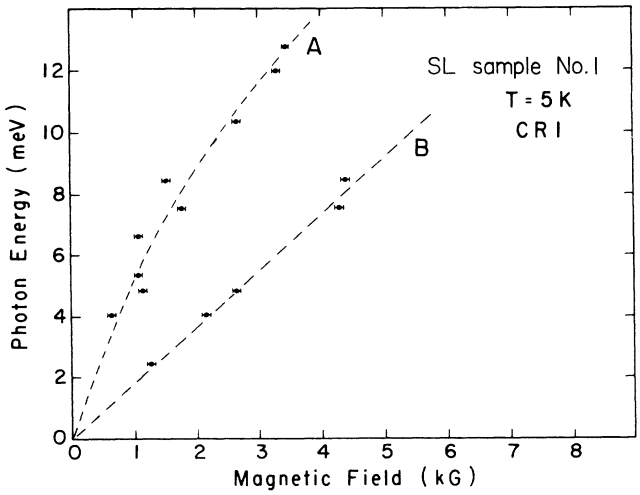

FIG. 6. A compilation of CRI results for SL sample No. 1 at 5 K. The points represent the positions of observed resonances for various laser wavelengths. Horizontal bars represent experimental error. The dashed line is merely a guide for the eye.

The magnetic field position of the weak line *B* in Fig. 6 is linear (within experimental error) and extrapolates smoothly to the origin. We do not at this time know the origin of this line.

The field positions versus photon energy for the resonance in the CRA polarization (line *C*) for SL sample No. 1 are plotted in Fig. 7. The dependence of line *C* is similar in both samples, and in both cases extrapolates to the origin in a very nonlinear fashion, again suggesting strong nonparabolicity of the band structure.

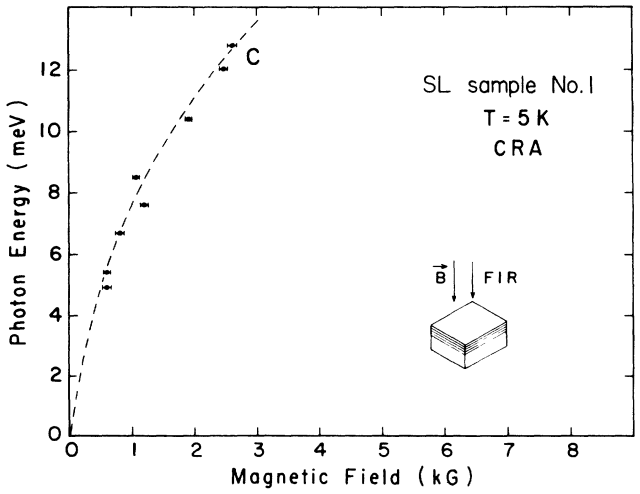

FIG. 7. FIR photon energies, as a function of magnetic fields for the resonances observed in the CRA circular polarization for the SL sample No. 1 at $T=5$ K. Horizontal bars represent experimental error, and the dashed line is a guide for the eye.

The temperature dependence of the spectrum observed in both circular polarizations is presented in Fig. 8. The data are taken for SL sample No. 1 at the wavelength $\lambda=229$ μm. Consider first the CRI polarization. The hole-cyclotron-resonance position (line *A*) shifts slightly to lower fields as the temperature increases. This behavior is clearly observed in both samples. The resonance intensity for both samples remains unchanged with increasing temperature until about 30 K, and no appreciable change in the resonance half-width is observed. At higher temperatures the intensity of resonance *A* begins to fall (above $T\approx 60$ K for SL sample No. 1 and above $T\approx 40$ K for SL sample No. 2), but the linewidth does not appear to broaden. The weak line *B* (barely discernible on the scale of Fig. 8) shifts to higher fields with increasing temperature and decreases in intensity, and until it disappears above $T=50$ K.

In the CRA polarization (*electron* cyclotron resonance active) the intensity of line *C* increases when the temperature is raised, and its position shifts slightly to higher fields. Above 30 K a new resonance emerges (line *D*), eventually "swallowing up" line *C* and dominating the CRA spectrum.

As we mentioned earlier, we identify line *A* as the cyclotron resonance of holes. The arguments supporting this interpretation are as follows. The transport measurements clearly show that our samples are *p* type at helium temperatures, so that holes are the majority carriers at low temperatures. Moreover, the resonance is excited by the circular polarization which corresponds to the cyclotron motion of holes.

Our interpretation will make use of Fig. 9, which shows the energy bands calculated for the parameters corresponding to one of our samples SL sample No. 2, $d_w=80$ Å, $d_b=40$ Å) at $B=1$ kG, using the transfer matrix algorithm developed by Ram-Mohan *et al.*[3] The calculated band structure is plotted as a function of the wave vector along the growth direction k_z. The level marked $-2'$ is very close in energy to the HH_1 band of Fig 2; it represents the bottom Landau level of the conduction band near $k_z=0$, and the top Landau level of the valence band near $k_z=\pi/d$. Similarly, the line marked "0" (which behaves similarly to the E_1 band in Fig. 2) represents the top Landau level of the valence band near $k_z=0$, and the bottom Landau level of the conduction band near the edge of the Brillouin zone. The small anticrossing "repulsion" of the levels seen at k_{zc}, which was shown in Fig. 2, is not present in Fig. 9 because the perturbation responsible for this interaction between levels was not included in the present calculation. This detail has no bearing on the problem except in the immediate vicinity of k_{zc}.

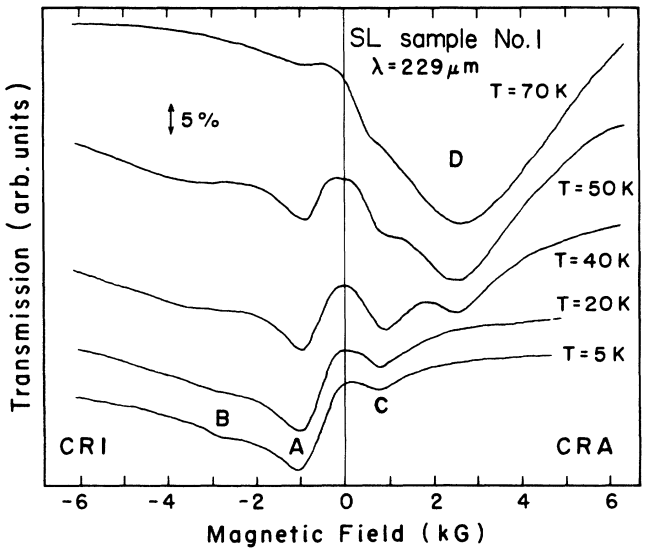

FIG. 8. The FIR magnetotransmission spectra obtained for the SL sample No. 1 in the Faraday geometry for both senses of circular polarization. The data were taken at $\lambda=229$ μm for several temperatures.

The excited Landau levels of the conduction band are shown by the group of continuous curves which originate above $-2'$ at $k_z=0$ and terminate above 0 at the zone edge. Similarly, the excited Landau levels of the valence band are those originating below the 0 level at $k_z=0$, and terminating below $-2'$ at $k_z=\pi/d$. The labeling sequence of the Landau states $(0,-2',1,-1'$, etc) is a matter of convention, consistent with Ref. 3. As can be seen from Fig. 2, the HH_1 band (and therefore the $-2'$ level) is very flat along the k_z direction, so that a large density of states is expected to be associated with it. The Fermi level must therefore lie close to the $-2'$ energy. Since the transport measurements indicate that at $T=5$ K both samples are *p* type, we draw the Fermi energy E_F (indicated on Fig. 9 as a dashed-dotted line) slightly below the $-2'$ level. (While we are confident that E_F lies below the $-2'$ level, note that it is less certain where E_F is located with respect to the excited Landau states at $B=0.1$ T.) Since the $-2'$ level is very flat, there are no favorable values of k_z for electrons and holes to occupy. We therefore expect the $-2'$ Landau subband electrons to contain some holes at random values of $k_z>k_{zc}$, as well as some electrons at arbitrary values of $k_z<k_{zc}$.

In terms of the picture shown in Fig. 9, we interpret line *A* as the cyclotron resonance of holes at (and near) $k_z=\pi/d$, as indicated by arrows marked "HCR" on the right of the figure. We emphasize that this transition probably involves a *range* of values of k_z near the zone edge, owing to the flatness of the $-2'$ level, the form of the resonance being ultimately determined by the density of states associated with the final state $(-1')$. As one can see, such a transition would not be possible at $k_z=0$, since both the initial and the final states are occupied with our choice of E_F.

Comparing the magnetoabsorption spectrum for both samples (see Fig. 5), one can also see that the integrated absorption for the hole cyclotron resonance (line *A*) for SL sample No. 1 is about ten times as large as for SL sample No. 2. The integrated absorption is directly proportional to the carrier concentration involved in the resonance process. This is consistent with galvanomagnetic data (see Table I), which indicate that the concentration of holes in SL sample No. 1 is an order of magnitude

higher than in SL sample No. 2. It should also be noted (see Fig. 5) that the hole cyclotron-resonance lines are very narrow, and are observable even at very low fields. The mobility estimated from their linewidths is of the order of 10^5 cm^2/V s, similar to our galvanomagnetic results. As can be seen from Fig. 8, there is no appreciable change in the resonance half-width as the temperature increases, again consistent with our galvanomagnetic data (see Fig. 3), indicating that the hole mobility (which is closely related to the resonance half-width) remains constant up to $T \approx 30$ K.

Using the relation $\omega = eB_c/m^*$, where B_c is the cyclotron resonance field, and ω is the FIR photon frequency, we find the effective masses for each magnetic field corresponding to line A, and extrapolate m^* to $B=0$. We find that at 5 K the effective masses of holes at $B=0$ are very light for both samples, as follows:

$m_0^*/m_0 = 0.0017$ for SL sample No. 1 ,

$m_0^*/m_0 = 0.0018$ for SL sample No. 2 .

We recall that these values may represent a *distribution* of in-plane masses for a range of k_z near π/d, which depends on the density of final states, as discussed earlier.

B. Cyclotron resonance of light (HH_1) electrons at low temperatures

The picture shown in Fig. 9 also permits us to identify the transition observed in the CRA polarization at low temperatures (labeled "C" in Figs. 5 and 8). We attribute this transition to the cyclotron resonance of *electrons* associated with the HH_1 band at and near $k_z = 0$ (indicated by "ECR" in Fig. 9). This attribution is supported by the temperature dependence of resonance C: when we raise the temperature, the initial state ($-2'$) becomes increasingly more populated, resulting in an increased resonance intensity, as seen in Fig. 8. Using the relation $\omega = eB_c/m^*$ for line C and extrapolating to $B=0$ we find that the electron in-plane effective masses for both superlattices are

$m_0^*/m_0 = 0.0017$ for SL sample No. 2 ,

$m_0^*/m_0 = 0.0012$ for SL sample No. 1 .

Observation of a larger mass in SL sample No. 2 indicates (as should be expected) that the magnitude of the (negative) Γ-point energy gap is larger for that sample.[13] The mobility estimated from the linewidth is of the order 10^5 cm^2/V s for both samples.

At this time we cannot say anything as to the origin of the higher field line observed in the CRI polarization (labeled B in Fig. 5). This line is very weak, and is only observed for the shorter FIR wavelengths. We therefore do not have sufficient data to attempt its identification.

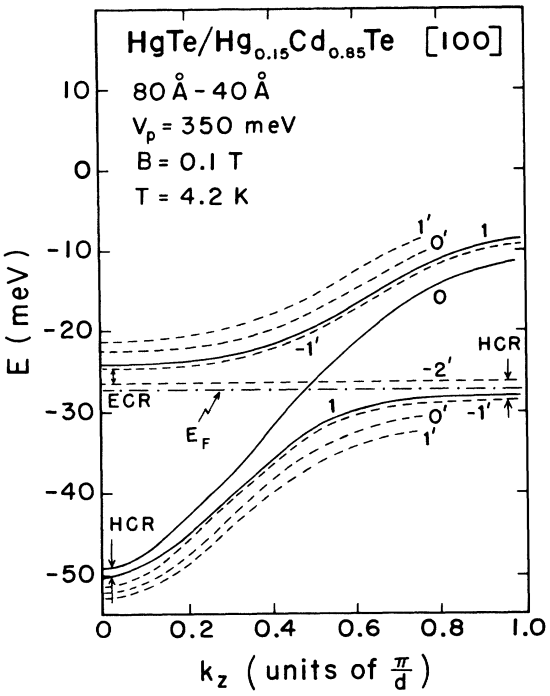

FIG. 9. Several lowest Landau levels calculated for zero-gap type-III superlattice as a function of the growth-direction wave vector k_z, for $B=0.1$ T and $T=4.2$ K (see text). The Fermi level is indicated by the dashed-dotted line. The hole cyclotron resonances (HCR's) and the electron cyclotron resonance (ECR) are indicated by arrows.

C. Cyclotron resonance of E_1 electrons at higher temperatures

As we increase the temperature above 20 K, a new resonance line is observed in the CRA circular polarization (labeled as resonance "D" in Fig. 8). This line gradually emerges near $T \approx 30$ K, and is the only line to survive above 100 K. We can still see the line at 200 K, which is the high-temperature limit of our measurements. The optical measurements performed at 300 K by Schulman *et al.*,[14] and FIR reflectivity measurements performed above 77 K by Kim *et al.*[15] on SL sample No. 1 indicate that at high temperatures this superlattice has a positive energy gap, such as is shown in Fig. 1. Since the galvanomagnetic data show that electrons strongly dominate electrical transport at high temperatures, we therefore interpret line D at temperatures above 70 K as the cyclotron resonance of electrons in the E_1 band.

The linewidth ΔB of resonance D depends on the FIR wavelength, but the ratio $\Delta B/B$ appears to remain constant for this line at any given temperature. The mobility estimated from the value of ΔB is $\mu \approx 9.6 \times 10^4$ cm^2/V s at $T=100$ K. The Hall mobility obtained from galvanomagnetic measurements for this sample is $\mu = 7 \times 10^4$ cm^2/V s for $T=100$ K, in very satisfactory agreement with the above estimate of μ. The linewidth ΔB for SL sample No. 2 is somewhat higher, suggesting a lower mobility for that sample ($\mu \approx 8 \times 10^4$ cm^2/V s), which again is consistent with the galvanomagnetic data.

Figure 10 shows the dependence of the magnetic field position of resonance D on photon energy at $T=100$ K for SL sample No. 1. As can be seen from the figure, the behavior is nonparabolic. However, the nonparabolicity is not as pronounced as was observed for the cyclotron resonance of holes and of the HH_1 electrons (see Figs. 6 and 7). The extrapolated zero-field effective mass corre-

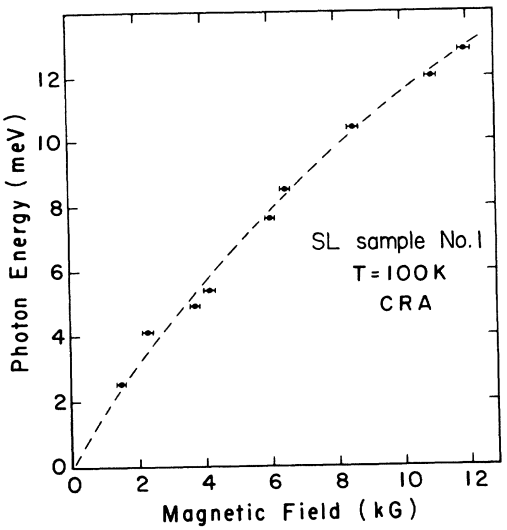

FIG. 10. Photon energy vs magnetic field for the cyclotron resonance of thermally excited electrons observed in the SL sample No. 1 at $T=100$ K. Horizontal bars represent experimental error, and the dashed curve is a guide for the eye.

sponding to the data in Fig. 10 is $m_0^*=0.006m_0$. We find that this value of m_0^* corresponds to a positive energy gap $Eg\approx 32.4$ meV.

Figure 11 shows the dependence of m^* on temperature (determined from the resonance field for $\lambda=229$ μm) for SL samples No. 1 and No. 2. Estimated energy gaps corresponding to several of the mass values are also shown in the figure. The estimates of the energy-gap values were obtained from the superlattice band-structure calculations for electrons $\frac{3}{2}k_BT$ above the bottom of the conduction band, and using the relation $m^*\equiv\hbar^2k(dE/dk)^{-1}$. As shown in the figure, the estimated energy gap for SL sample No. 1 at $T=200$ K is $E_g\approx 40$ meV. This value is consistent with the room-temperature energy gap of ≈ 70 meV, obtained from optical measurements at 300 K for this sample by Schulman *et al.*[14] Note that the temperature dependence of the effective mass is similar for both samples. At 200 K both samples have positive Γ-point energy gaps ($E_1>HH_1$) which are expected to decrease with decreasing temperature. The effective masses are thus also expected to decrease along with the energy gaps.

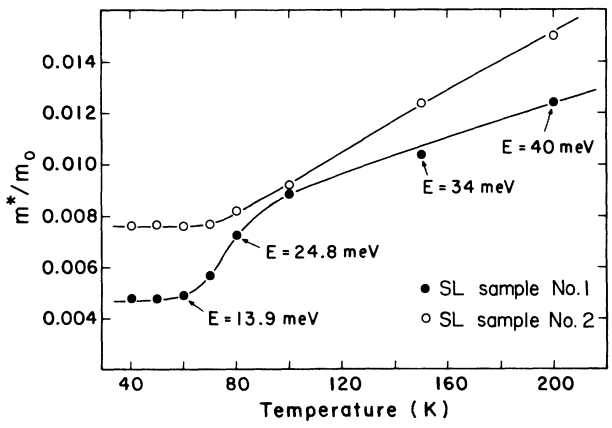

FIG. 11. Temperature dependence of the electron effective masses (E_1 band) for both samples obtained from the cyclotron-resonance data. The points are experimental, obtained at $\lambda=229$ μm. The energies E indicated in the figure are energy gaps estimated for various temperatures. The line is a guide for the eye.

Around 80 K, however, we observe a sudden jump in the mass behavior (clearly seen for SL sample No. 1), and below 60 K the values of the effective mass show no further change with temperature. We believe that this is the region (between 40 and 70 K) where the gap at $k_z=0$ is near zero. In this region both lines C and D are observable at the same time. As long as the energy gap is near zero (i.e., when E_1-HH_1 at the Γ point is either positive or negative, but very small), there is a strong interband interaction, and the entire picture becomes very complicated. A detailed calculation for the band structure in the presence of a magnetic field is required to understand the magneto-optical transitions in this region. Unfortunately our data cannot accurately determine the temperature for which the transition from the zero gap ($E_1<HH_1$) to the open gap situation ($E_1>HH_1$) occurs. However, on the basis of the "knee" in the curves shown in Fig. 11, one might expect that for SL sample No. 1 that transition takes place below $T=60$ K, and for SL sample No. 2 below $T=70$ K.

D. Anisotropy of cyclotron resonance data

We now discuss the anisotropy of the cyclotron resonances of both holes and electrons. In addition to measurements in the Faraday geometry discussed above, we have performed experiments in the Voigt geometry, in which the magnetic field **B** is perpendicular to the growth direction and to the direction of wave propagation **k**. In this geometry cyclotron orbits involve motion normal to the superlattice layers for part of the orbit. In order to establish the relationship of the absorption lines observed in the Faraday and Voigt geometries, we have carried out systematic measurements in which we tilted the samples so that **B** is at an angle θ to the growth direction. The Voigt and tilted geometry measurements were carried out at $\lambda=118.8$, 163, 229, and 496 μm.

Figure 12 presents the experimental data for SL sample No. 1 for $\lambda=229$ μm and $T=100$ K for several values of the angle θ, for incident polarization $\mathbf{E}\perp\mathbf{B}$. As indicated in the figure, θ is the angle between the magnetic field and the growth direction. It should be recalled from Sec. C, above, that at $T=100$ K the only absorption line observed in the Faraday geometry is the cyclotron resonance of electrons in the E_1 band, as can be seen from Fig. 8, CRA polarization. The magnetic field position of this Faraday-geometry resonance (corresponding to $\theta=0$, i.e., involving in-plane cyclotron motion) is indicated in Fig. 12 by an arrow (bottom of figure, near 3 kG). We can see from the figure that the position of the resonance line is strongly dependent on the orientation of B with

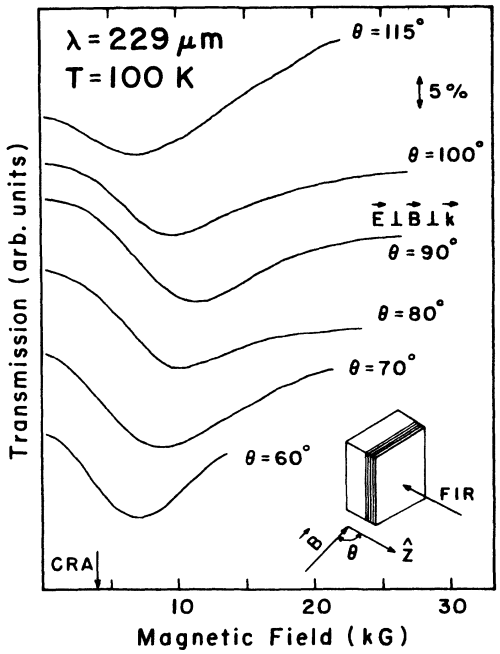

FIG. 12. FIR magnetotransmission spectra for the SL sample No. 1 at a fixed laser wavelength $\lambda=229$ μm and temperature $T=100$ K, for various values of θ, the angle between the magnetic field **B** and the growth direction $\hat{z}$. The incident polarization **E** is perpendicular to **B**. $\theta=90°$ corresponds to the **E**⊥**B** Voigt geometry. The arrow at the bottom indicates the field at which cyclotron resonance is observed in the Faraday geometry for CRA polarization.

respect to the superlattice layers (i.e., that the effective mass is anisotropic). Also apparent from Fig. 12 is that the resonance line is well defined for every angle, so that the resonance position can be established reliably for each orientation.

To analyze this behavior, we have used the assumption that the constant energy surface of the electrons is an ellipsoid of revolution. For that case the cyclotron-resonance effective mass is given by

$$\frac{1}{m^2(\theta)}=\frac{\cos^2\theta}{m_x^2}+\frac{\sin^2\theta}{m_x m_z}\ , \tag{1}$$

where m_x and m_x are the effective masses in the superlattice layers and along the growth direction, respectively. We have found that in the case of electrons this form of anisotropy works very well (i.e., m_z/m_x is independent of θ within experimental error).

Using Eq. (1) and experimental effective masses $m(\theta)$ corresponding to the Faraday and to the Voigt resonance fields, we obtain the m_z values and the m_z/m_x ratios given in Table II for several temperatures. The m_z/m_x ratio is seen to decrease systematically with temperature, and does not depend on the phonon energy in the range $118.8<\lambda<496$ μm. We note from the table that the smaller the in-plane (m_x) mass, the larger is the anisotropy (i.e., the larger is the m_z/m_x ratio). The temperature dependences of the parallel and perpendicular effective

TABLE II. Electron mass anisotropy.

T	m_z/m_0	m_x/m_0	m_z/m_x	m_z/m_x (theory)
50	0.100±0.01	0.0053	18.9	10.5
60	0.088±0.01	0.0052	16.9	8.3
70	0.080±0.01	0.0057	14.0	7.4
80	0.075±0.01	0.0064	11.7	6.7
100	0.065±0.01	0.0080	8.1	5.8
120	0.052±0.01	0.0095	5.5	5.2
150	0.040±0.01	0.0120	3.3	4.7

masses are shown in Fig. 13. Note that these results are in agreement with the recent magneto-optical determination of the electron mass anisotropy in n-type $Hg_{1-x}ZnTe$-CdTe superlattices by Berroir *et al.*[16] The authors in Ref. 16 have additionally demonstrated that the mass anisotropy ratio increases very rapidly with the CdTe layer thickness, as should perhaps be intuitively expected (the greater the barrier thickness, the greater the value of m_z).

We should point out that in the above discussion we have used the straightforward interpretation of the cyclotron resonance anisotropy, i.e.,

$$\omega_c(\theta)=eB(\theta)/m(\theta)\ , \tag{2}$$

with $m(\theta)$ given by Eq. (1), i.e., we have ignored the possibility of a plasma shift of the resonance for $\theta\neq0$. Our

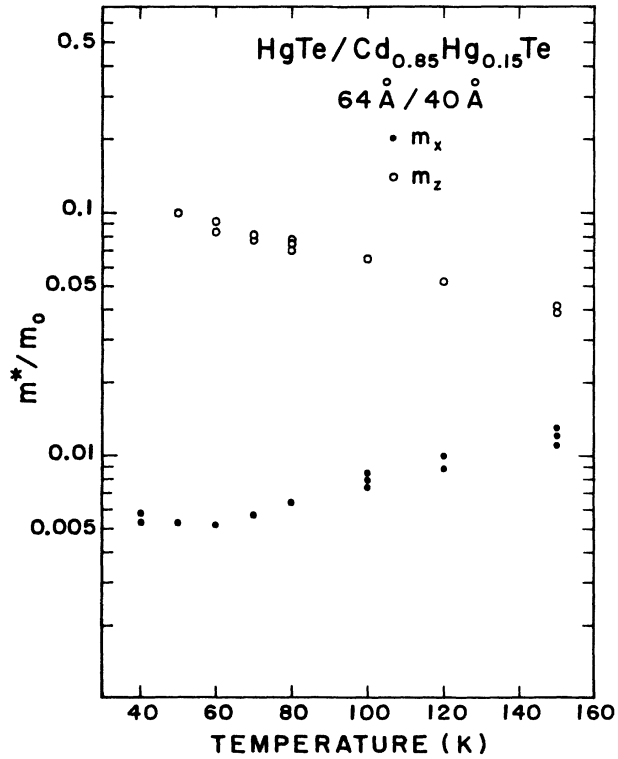

FIG. 13. Temperature dependence of the in-plane m_x^* and growth-direction m_z^* effective masses obtained for SL sample No. 1. Vertical bars indicate errors. All data are taken at the laser wavelength $\lambda=229$ μm except for the points at $T=60$ K, which were obtained at $\lambda=496$ μm.

basis for doing so is the fact that the position of the resonance in the extraordinary Voigt geometry (**B** in the plane of the sample, **E**⊥**B**, $\theta=90°$) follows the behavior predicted by Eq. (2), rather than the plasma-shifted behavior

$$\omega=(\omega_c^2+\omega_p^2)^{1/2}\ , \tag{3}$$

where ω_p is the plasma frequency. That is, as stated earlier, the effective mass m_z obtained from the Voigt data is independent of the photon energy, within experimental error.

Table II also gives *theoretical* estimates for the mass anisotropy, where it has been assumed that the Γ-point energy gap crosses zero at 60 K. One finds that the agreement between theory and experiment is qualitatively quite good. Quantitatively, however, the theory predicts that m_z should have a weaker temperature dependence than is indicated by the experimental results.

In determining the anisotropy of the hole masses, the results are not as accurate as for electrons. Unfortunately, the resonances observed in the Voigt (**E**⊥**B**) geometry at low temperatures are extremely broad, and thus poorly defined. However, we can conclude that the effective mass of the HH_1 holes in the growth direction is about 2 orders of magnitude heavier than the in-plane mass. This is in agreement with the recent results of Perez *et al.*[8] We can also conclude that, in contrast to the E_1 electrons, for HH_1 holes the assumption of an ellipsoidal constant energy surface does not hold, i.e., the angular dependence of ω_c which we observe does not follow Eq. (1).

Finally, our results indicate that the ratio m_z/m_x for the HH_1 holes also depends on the temperature. For example, for SL sample No. 1 at $T=5$ K, $m_z/m_x\approx 140$, while at $T=30$ K, $m_z/m_x\approx 230$. As can be seen from Figs. 1 and 2, such high anisotropy is consistent with the model that assumes a valence-band offset of ≈350 meV, in that this model predicts a heavy-hole band which is almost dispersionless in the k_z direction.

E. $1s\rightarrow 2p$ transitions and cyclotron resonance in the substrate

In addition to the resonances described above, we observed two very strong and broad absorption lines which occur in only one of the samples, SL sample No. 2. One of these lines is shown in Fig. 14. The data are taken for the CRA polarization at $T=5$ K for several laser wavelengths. This line occurs in the low-temperature range, and only for wavelengths $\lambda\leq 118.8$ μm One can see that its intensity is orders of magnitude stronger than that of line *C* observed at longer wavelengths.

Figure 15 shows the magnetic field position of this line as a function of photon energy. The striking feature of this transition is that, for $B=0$, the energy clearly extrapolates to $E=10.4$ meV. As the temperature increases, the energy intercept for $B=0$ remains almost unchanged with temperature, but the intensity of the line gradually decreases and disappears when T is greater than 80 K. One of the most important characteristics of this line is that it is *isotropic*, i.e., its position is insensitive to rotation of the sample relative to the direction of **B**.

When the temperature is raised above 15 K, a new line

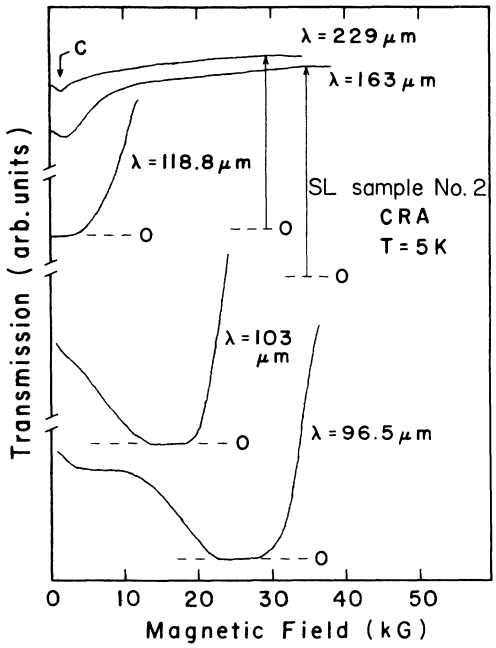

FIG. 14. FIR magnetotransmission spectra obtained on SL sample No. 2 in the Faraday geometry for the CRA circular polarization. The data are taken at $T=5$ for several photon wavelengths. The zero levels for each transmission spectrum are indicated by horizontal dashed lines.

emerges at high magnetic fields for longer wavelengths ($\lambda\geq 229$ μm) in the CRA polarization. Again, this new line is observable only in SL sample No. 2. At $T=15$ K we can see only a shadow of the line, but it rapidly gains in intensity as the temperature is increased. At temperatures above 70 K it becomes a very strong and broad resonance which dominates the spectrum, as can be seen from Fig. 16. The magnetic field position of the line does not depend on the temperature. It depends linearly on the photon energy, and extrapolates to the origin. Again,

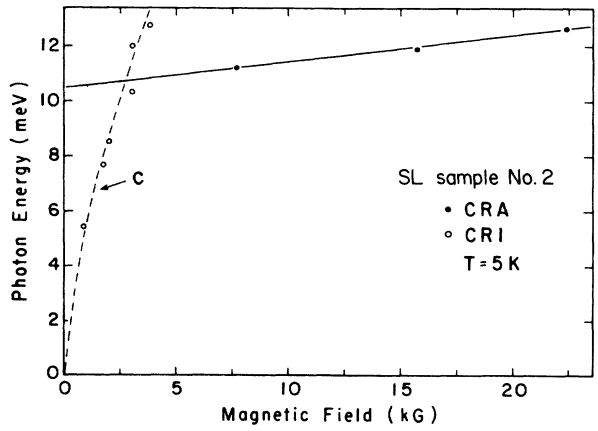

FIG. 15. A compilation of the Faraday geometry data for SL sample No. 2. The lines provide a guide for the eye, showing that the high-field line has a finite zero-field intercept energy $E\approx 10.4$ meV.

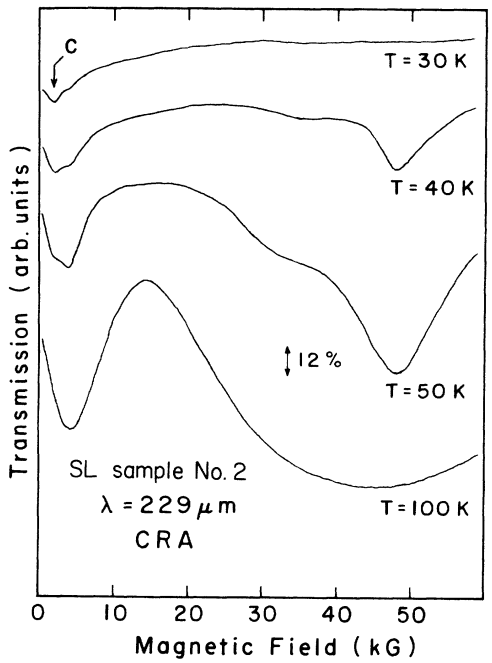

FIG. 16. FIR magnetotransmission spectra obtained on SL sample No. 2 in the Faraday geometry for the circular CRA polarization. The data are taken for $\lambda=229$ μm, for several temperatures. Note the high-field line, which emerges at $T=40$ K and gains its intensity with increasing temperature. We identify this line as the cyclotron resonance of thermally excited electrons in the CdTe substrate of the superlattice.

one of the most important characteristics of this line is that its position is insensitive to rotation of the sample relative to the direction of **B**. The fact that both of the lines just described are isotropic suggest that they are not affected by quantum confinement in the growth direction, i.e., they do not originate from the superlattice.

We attribute the strong, low-temperature line to the $1s \rightarrow 2p^+$ transition within shallow donor states in the CdTe substrate. The energy separation between the $1s$ ground state and the $2p$ excited state of a hydrogenlike donor is equal to

$$E_{2p}-E_{1s}=3/4R^* ,$$

where $R^*=(m^*/m_0)R_H/\kappa$, κ is the static dielectric constant, and R_H is the hydrogenic Rydberg. Our zero-field extrapolation energy of 10.4 meV is identical to the value of the $1s \rightarrow 2p$ transition obtained by Wagner and McCombe for CdTe.[18]

The line which appears above $T=15$ K in the high magnetic field region is cyclotron resonance of thermally excited electrons in the CdTe substrate. From the temperature dependence of the integrated absorption of the cyclotron resonance observed at $B=4.62$ T we find the activation energy of this line to be $E=16\pm1$ meV. This value is in very good agreement with the ionization energy for a shallow donor in CdTe, which for the magnetic field $B=4.62$ T is 16.6 meV. The line position indicates an effective mass of $0.0989m_0$ at $\lambda=229$ μm, in excellent agreement with the electron mass obtained by others from cyclotron-resonance measurements on bulk CdTe for the same field.[19]

To verify the assumption that the two strong lines originate from the CdTe substrate of SL sample No. 2, after completion of the study we cleaved off a piece of the sample, etched away the superlattice on the cleaved-off portion, and repeated the magnetotransmission experiments on the bare substrate. The two resonances ($1s \rightarrow 2p^+$ transition and electron cyclotron resonance of CdTe) remained as strong as before, and the rest of the resonances disappeared, verifying the interpretation just made.

V. CONCLUSIONS

The FIR magnetotransmission as well as galvanomagnetic measurements on two zero-band-gap $HgTe/Cd_{0.85}Hg_{0.15}Te$ superlattices [64 Å/40 Å and 80 Å/40 Å] grown on (100)-oriented CdTe substrates were performed over a wide range of temperature (5 K $\leq T \leq$ 200 K). Six types of resonances of different origins were observed. By correlating the FIR measurements with the galvanomagnetic data, we were able to identify three of the resonances: in the low-temperature region ($T<40$ K), where the superlattices are characterized by a zero energy gap, we observe the cyclotron resonance of extremely light holes originating from the HH_1 band near $k_z=\pi/d$, and of electrons in the HH_1 band at $k_z=0$. The values of the hole masses are consistent with a large value of the valence-band offset ($\approx$350 meV). At high temperatures ($T>70$ K), where the samples are characterized by a positive gap ($E_1>HH_1$), we identify one of the observed lines as the cyclotron resonance of thermally excited electrons in the E_1 band. Furthermore, two of the remaining resonances were identified as the $1s \rightarrow 2p^+$ transition associated with donors and as the electron cyclotron resonance, both occurring in the CdTe substrate of one of the superlattices. Finally, one weak resonance still remains unidentified.

Our data provide information on the effective-mass anisotropy of the conduction electrons and holes in the superlattice, and on its temperature dependence. We have attempted to correlate the observed temperature dependence of the effective-mass properties with the temperature-induced transition of the superlattice from the zero-band-gap to the open-band-gap situation. However, detailed analysis of the data just presented requires magnetic-field-dependent superlattice band-structure calculations for the superlattice, both for the Faraday and the Voigt geometries. These are currently being pursued.

ACKNOWLEDGMENTS

The authors are very grateful to L. R. Ram-Mohan for making available to us his **k·p** algorithm which permitted us to calculate Fig. 9, and for many valuable discussions. We also acknowledge the support of the National Science Foundation Grant No. DMR-8904802.

[1]C. A. Hoffman, J. R. Meyer, F. J. Bartoli, J. W. Han, J. W. Cook, Jr., J. F. Schetzina, and J. N. Schulman, Phys. Rev. B **39**, 5208 (1989).
[2]J. R. Meyer, C. A. Hoffman, F. J. Bartoli, J. W. Han, J. W. Cook, Jr., J. F. Schetzina, X. Chu, J. P. Faurie, and J. N. Schulman, Phys. Rev. B **38**, 2204 (1988).
[3]L. R. Ram-Mohan, K. H. Yoo, and R. L. Aggarwal, Phys. Rev. B **38**, 6151 (1988).
[4]J. Tersoff, Phys. Rev. Lett. **56**, 2755 (1986).
[5]Y. Guldner, G. S. Boebinger, J. P. Vieren, M. Voos, and J. P. Faurie, Phys. Rev. B **36**, 2958 (1987).
[6]Z. Yang, M. Dobrowolska, H. Luo, J. K. Furdyna, J. T. Cheung, and N. Otsuka, App. Phys. Lett. **55**, 380 (1989).
[7]Z. Yang, M. Dobrowolska, H. Luo, J. K. Furdyna, and J. T. Cheung, Phys. Rev. B **38**, 3409 (1988).
[8]J. M. Perez, R. J. Wagner, J. R. Meyer, J. W. Han, J. W. Cook, Jr., and J. F. Schetzina, Phys. Rev. Lett. **61**, 2261 (1988).
[9]J. N. Schulman and Y.-C. Chang, Phys. Rev. B **33**, 2594 (1986).
[10]J. M. Berroir, Y. Guldner, J. P. Vieren, M. Voos, and J. P. Faurie, Phys. Rev. B **34**, 891 (1986).
[11]Y. Guldner, G. Bastard, J. P. Vieren, M. Voos, J. P. Faurie, and A. Million, Phys. Rev. Lett. **51**, 907 (1983).
[12]N. F. Johnson, P. M. Hui, and H. Ehrenreich, Phys. Rev. Lett. **61**, 1993 (1988).
[13]The theory predicts that E_1 and HH_1 in-plane masses depend approximately linearly on the magnitude of the energy separation between the two bands.
[14]J. N. Schulman, O. K. Wu, E. A. Patten, J. W. Han, Y. Lansari, L. S. Kim, J. W. Cook, Jr., and J. F. Schetzina, Appl. Phys. Lett. **54**, 745 (1989).
[15]L. S. Kim, S. Perkowitz, and O. K. Wu, Bull. Phys. Soc. **34**, 1002 (1989).
[16]J. M. Berroir, Y. Guldner, J. P. Vieren, M. Voos, X. Chu, and J. P. Faurie, Phys. Rev. Lett. **62**, 2024 (1989).
[17]T. Duffield, R. Bhat, M. Koza, F. DeRosa, D. M. Hwang, P. Grabbe, and S. J. Allen, Jr., Phys. Rev. Lett. **56**, 2724 (1986).
[18]R. J. Wagner and B. D. McCombe, Phys. Status Solidi B **64**, 205 (1974).
[19]C. W. Litton, K. J. Button, J. Waldman, D. R. Cohn, and B. Lax, Phys. Rev. B **13**, 5392 (1976).